PNAS RESEARCH ARTICLE | PHYSICS

Unifying the order and disorder dynamics in photoexcited VO_2

Hao-Wen Liu[a,b,1], Wen-Hao Liu[a,b,1], Zhao-Jun Suo[a,b], Zhi Wang[a], Jun-Wei Luo[a,b,2], Shu-Shen Li[a,b], and Lin-Wang Wang[c,2]

Edited by Jianming Cao, Florida State University, Tallahassee, FL; received December 18, 2021; accepted May 27, 2022 by Editorial Board Member Zachary Fisk

Photoinduced phase transition (PIPT) is always treated as a coherent process, but ultrafast disordering in PIPT is observed in recent experiments. Utilizing the real-time time-dependent density functional theory method, here we track the motion of individual vanadium (V) ions during PIPT in VO_2 and uncover that their coherent or disordered dynamics can be manipulated by tuning the laser fluence. We find that the photoexcited holes generate a force on each V–V dimer to drive their collective coherent motion, in competing with the thermal-induced vibrations. If the laser fluence is so weak that the photoexcited hole density is too low to drive the phase transition alone, the PIPT is a disordered process due to the interference of thermal phonons. We also reveal that the photoexcited holes populated by the V–V dimerized bonding states will become saturated if the laser fluence is too strong, limiting the timescale of photoinduced phase transition.

photoinduced phase transition | order and disorder dynamics | rt-TDDFT

Significance

Structural phase transitions driven optically through the nonequilibrium population of excited electronic states have attracted great interest in many scientific disciplines as offering ultrafast control over the matter on timescales near the limit of atomic motions. However, atomic order or disorder characteristics are currently a critical issue in ultrafast photoinduced phase transitions. In this work, using an advanced real-time time-dependent density functional theory quantum simulation, we uncover the order and disorder processes strongly depending on the competition between thermal vibrations and photoinduced deterministic motion of atoms. We theoretically unify the order and disorder dynamics and provide a complete microscopic mechanism.

Photoexcitation using ultrafast laser pulses provides a powerful approach to manipulate the material properties with a timescale in the limit of atomic motion (1–9). It was believed that the atomic motion in the photoinduced phase transitions (PIPTs) is in collective coherent dynamics (10–13). However, recent experiments show an ultrafast disordering of atomic motions in PIPTs of VO_2 (14) and $Rb_{0.3}MoO_3$ (15), challenging the conventional view of phase transitions. As an archetypical 3*d*-correlated oxide (16, 17), manipulating the transition from the monoclinic (M_1) insulator phase to the rutile (R) metallic phase in VO_2, as shown in Fig. 1 *A* and *D*, is a popular topic with numerous efforts that have focused on elucidating the evolution of both the electronic and lattice degrees of freedom. Photoinduced insulator-to-metal transition is ultrafast with subfemtosecond timescales (18, 19). Using a four-dimensional femtosecond electron diffraction to measure the evolution of the V–V dimers following the photoexcitation, Baum et al. (20) discovered that the motion of the V atoms is first along the direction of the V–V bond (*a* axis) with femtosecond timescales, then along the *b* and *c* axis within picosecond timescales, thus claiming a coherent structural transition from M_1 to R phase. In addition, some experimental groups have reported that the PIPT in VO_2 originates from a coherent motion of V–V dimers at 6-THz phonon mode (10, 21–23). However, in a recent experiment, Wall et al. (14) used a femtosecond total X-ray scattering method beyond the general X-ray or electron diffraction (2, 12, 20, 24–26) to measure averages over many unit cells and they discovered the motion of V–V dimers is disordered in PIPT rather than a collective motion along the coherent phonon coordinate.

In addition to the debate of atomic ordering or disordering in the phase transition, the timescale of M_1-to-R phase transition in VO_2 also has a major controversy. Early experiments reported the timescale of PIPT being gradually reduced from 100 fs to 40 fs (18) with increasing laser fluence (10, 18, 19). However, Otto et al. (25) recently observed far longer timescales of 200 to 500 fs without apparent relation with the laser fluence. This has been attributed to disordered movements of the atoms, thus Otto et al. supported that the PIPT in VO_2 should be viewed as a disordering or even melting transition (25). How to consolidate these different experimental claims, both in order and disorder phase transition and in their corresponding timescales, is thus a major challenge in this field.

In this work, to investigate the coherent or disordered manner of atomic motion, we have utilized our newly developed real-time time-dependent density functional theory (rt-TDDFT) algorithm (6, 27, 28) to simulate the PIPT in VO_2. We show that the phase transition is in atomic disordering with a timescale of ∼200 fs at low laser fluence. Whereas, at high laser fluence, it becomes a coherent manner with a fluence-dependent timescale below 100 fs. The disordering phase transition is driven by a combination of the atomic driving forces caused by photoexcitation and thermal phonon

Author affiliations: [a]State Key Laboratory of Superlattices and Microstructures, Institute of Semiconductors, Chinese Academy of Sciences, Beijing 100083, China; [b]Center of Materials Science and Optoelectronics Engineering, University of Chinese Academy of Sciences, Beijing 100049, China; and [c]Materials Science Division, Lawrence Berkeley National Laboratory, Berkeley, CA 94720

Author contributions: J.-W.L. and L.-W.W. designed research; H.-W.L. and W.-H.L. performed research; H.-W.L., W.-H.L., Z.-J.S., Z.W., J.-W.L., S.-S.L., and L.-W.W. contributed new reagents/analytic tools; H.-W.L., W.-H.L., J.-W.L., and L.-W.W. analyzed data; H.-W.L., W.-H.L., J.-W.L., and L.-W.W. wrote the paper; and S.-S.L. provided the project infrastructure and supervised H.-W.L.'s study.

The authors declare no competing interest.

This article is a PNAS Direct Submission. J.C. is a guest editor invited by the Editorial Board.

[1]H.-W.L. and W.-H.L. contributed equally to this work.

[2]To whom correspondence may be addressed. Email: jwluo@semi.ac.cn or lwwang@semi.ac.cn.

This article contains supporting information online at http://www.pnas.org/lookup/suppl/doi:10.1073/pnas.2122534119/-/DCSupplemental.

Published July 6, 2022.

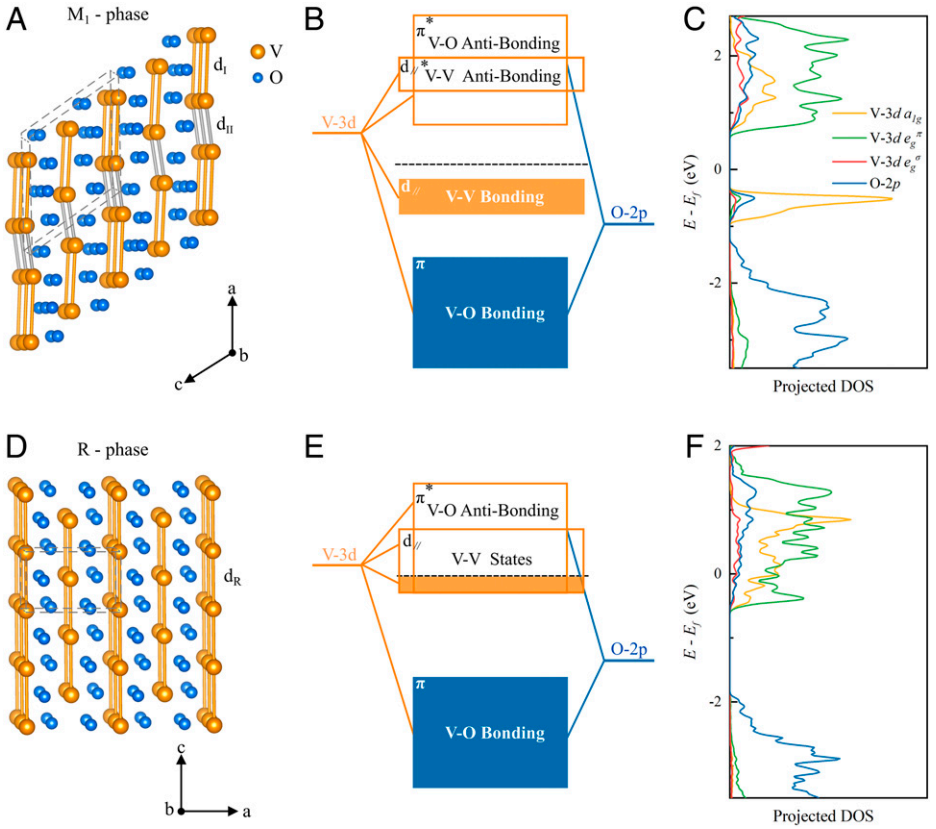

Fig. 1. VO_2 atomic and electronic structures. (*A*) The 2 × 2 × 2 supercell structure of M_1-phase VO_2 in which d_I and d_{II} represent the V–V long and short bonds. Gray parallelepipeds represent the unit cell of the VO_2 structures. V and O atoms are labeled with orange and blue balls, respectively. (*B*) Schematic of the VO_2 bonding and antibonding states of M_1-phase VO_2. (*C*) The projected density of states (PDOS) of M_1-phase VO_2. (*D*) The 2 × 2 × 4 supercell structure of R-phase VO_2 in which all V–V bonds (d_R) are equal. (*E*) Schematic of the VO_2 bonding and antibonding states of R-phase VO_2. (*F*) The PDOS of R-phase VO_2.

vibration. On the other hand, the coherent phase transition is predominantly controlled by the photoexcited atomic driving forces, and the thermal phonon is only a small perturbation. We also demonstrate that, with increasing the laser fluence, the smallest timescale of phase transition is indeed saturated to a minimum value of ∼55 fs, which is due to the saturation of the population of the V–V bonding states by the photoexcited holes. Our findings provide a unified theory for understanding the atomic coherent and disordering motion in PIPT, uniting different experimental results.

Results

Atomic Structures and Electronic Orbital Properties. At high temperature, VO_2 is stabilized in a high-symmetry R phase ($P4_2/mnm$) with a vanadium atom surrounded by six oxygen atoms forming an octahedron. When the temperature is below the transition temperature $T_c \sim 340$ K (29, 30), the vanadium atoms deviate from the octahedral geometric center to form a low-symmetry M_1 phase ($P2_1/C$). The V–O octahedral environment and the coupling between the O 2*p* orbitals and V 3*d* orbitals split the V 3*d* orbitals into a combination of low-energy triply degenerate t_{2g} states ($d_{x^2-y^2}$, d_{xz} and d_{yz}) and high-energy doubly degenerate e_g^σ states (d_{z^2} and d_{xy}) (31, 32). The t_{2g} states are further separated into an a_{1g} orbital ($d_{x^2-y^2}$) and two e_g^π orbitals (d_{xz} and d_{yz}) because of the V–O octahedral structure with different V–O distances (which breaks the cubic symmetry). Notably, the a_{1g} orbital is parallel to the rutile *c* axis (c_R), thus it hardly hybridizes with O 2*p* orbitals to form V–O bonds. The dimerization of the V atoms leads to twisted V–V pairs, splitting the highly directional a_{1g} orbital into a bonding state ($d_\parallel$) and an antibonding state ($d_\parallel^*$) (Fig. 1 *B* and *C*). The antibonding orbital energy is raised over the original orbital energy by an amount *V* (usually referred to as the overlap parameter), the same as the bonding orbital energy decrease (33). Manipulating the electrons on the $d_\parallel$ bonding state to occupy the $d_\parallel^*$ antibonding state by photoexcitation can break the V–V dimers, inducing an M_1-to-R phase transition.

Coherence and Disordering of Atomic Motion. To simulate the photoinduced M_1-to-R ultrafast phase transition, we utilize an 800-nm laser to pump electrons from valence bands to conduction bands of VO_2 in our rt-TDDFT simulations. The initial lattice temperature is set to 50 K. In photoexcited simulations, we use an external electric field with a Gaussian shape (*SI Appendix*, Fig. S2*A*),

$$E\ (t) = E_0\cos(\omega t)\exp[-(t - t_0)^2/(2\sigma^2)], \qquad [1]$$

to simulate the laser pulse. Here, $t_0 = 17.5$ fs, pulse width $\sqrt{2}\sigma = 7$ fs, and photon energy $\hbar\omega = 1.02$ eV (see *Materials and Methods*). In addition, we use E_0 to tune the laser fluence. With increasing E_0 from 0 to 0.5, the photoexcited electrons from the valence band to the conduction band gradually increase from 0 to 6.3% of the valence electrons (*SI Appendix*, Fig. S2*B*). In addition, we also simulate the PIPT processes with the photon energy $\hbar\omega = 1.55$ eV (*SI Appendix*, Figs. S13 and S14), which is consistent with experimental parameters

(14, 25). The PIPT processes in VO_2 are identical under the two different photon excitations.

We show the evolution of V–V bonds to track the M_1-to-R phase transition in Fig. 2*A* and *SI Appendix*, Fig. S3*A*. In the M_1 phase, V atoms deviate from the oxygen octahedral center so that V atoms have two types of V–V bonds, including a group of long V–V bonds (d_I) and a group of short V–V bonds (d_{II}) called V–V dimers. All V–V bonds (d_R) have the same value in the R phase. The V–V long bonds (d_I = 3.21 Å) and the V–V short bonds (d_{II} = 2.51 Å) gradually become equal ($d_I = d_{II} = d_R$ = 2.84 Å) with time evolution in our simulations, representing the process of the photoinduced M_1-to-R phase transition, as shown in Fig. 2*A* and *SI Appendix*, Fig. S3*A*. Thus, we define the first time when the d_I and d_{II} become equal as the phase transition time τ. The residual atomic kinetic energy drives the atomic movement along the original movement direction after τ and leads to a damping oscillation on a timescale longer than 1 ps, as shown in *SI Appendix*, Fig. S4. We discover that there are different types of dynamic processes with different photoexcitation levels. At low electronic excitations (percentage of excited electrons η = 1.0%), the changes in individual long bonds and individual short bonds during PIPT are not all the same. Rather, their changes can be characterized as disordered motions, and the phase transition time τ is nearly 187 fs. With increasing laser fluence, d_I and d_{II} can rapidly become the same within 100 fs, and the motions of all bonds are nearly synchronous and hence can be characterized as coherent dynamics.

To describe the degree of disorder in atomic motion, we define a disorder parameter ($L_{disorder}$):

$$L_{disorder} = \sum_{i=1}^{n} \sqrt{(x_i - x_{ave})^2 + (y_i - y_{ave})^2 + (z_i - z_{ave})^2}/n. \quad [2]$$

The summation runs over V-V bonds, and n represents the number of V–V bonds. x_i, y_i, and z_i represent the V–V bond length in the x, y, and z directions. x_{ave}, y_{ave}, and z_{ave} represent the average V–V bond length in the x, y, and z directions. Fig. 2*B* and *SI Appendix*, Fig. S3*B* show the $L_{disorder}$ change within the timescale of the phase transition in different electronic excitations. At 1.0% electronic excitation, the disordered degree rapidly reached 0.2 Å before the M_1-to-R phase transition. However, the disorder degrees are less than 0.1 Å during PIPT in other higher excitations. Remarkably, the higher electronic excitation does not increase the disorder at the phase transition point, and it decreases it slightly. We can thus conclude that electron excitation does not induce disorder. We next proceeded with the fast Fourier transform (FFT) for V–V bonds to obtain phonon modes of V atomic motion. Three low-frequency phonon modes from atomic vibrations are discovered at 0.7, 1.8, and 2.9 THz at 1.0% excitation (Fig. 2*C*). The multiple phonon modes with three peaks further confirm the disordered process of the phase transition at 1.0% excitation. We only find a single peak between 4 and 5.5 THz at all higher excitations (Fig. 2*C* and *SI Appendix*, Fig. S3*C*). These high-frequency modes are generally called coherent phonons in the experimental literature (10, 21, 22), and they are attributed to the coherent PIPT.

The disorder degree described in Fig. 2*B* and the intensity of diffuse scattering in the experiment (14) have the same physical meaning, representing the degree of disorder of the atoms in the system. The intensity of diffuse scattering in the experiment shows a consecutive enhancement when the fluence increase from 0 to 22 mJ/cm^2. They found the strongest fluence of 22 mJ/cm^2 in the experiment excites 0.9% of valence electrons to the empty conduction bands, which was taken into account in their ab initio molecular dynamic (AIMD) simulations by setting artificially the electronic temperature to T_{el} = 2,204 K. For a better comparison to the experimental data, we have proceeded with some simulations at below 1.0% electronic excitation (<24 mJ/cm^2). The dynamic evolutions of bond length and the corresponding disorder degree over time are shown in *SI Appendix*, Fig. S5. To assess the dependence of disorder degree against the laser fluence, Fig. 3 shows the evolution of the maximum disorder degree within 400 fs for electronic excitations from 0 to 2.3%. Our simulations reproduce the experimental observation that the disorder degree gradually raises as

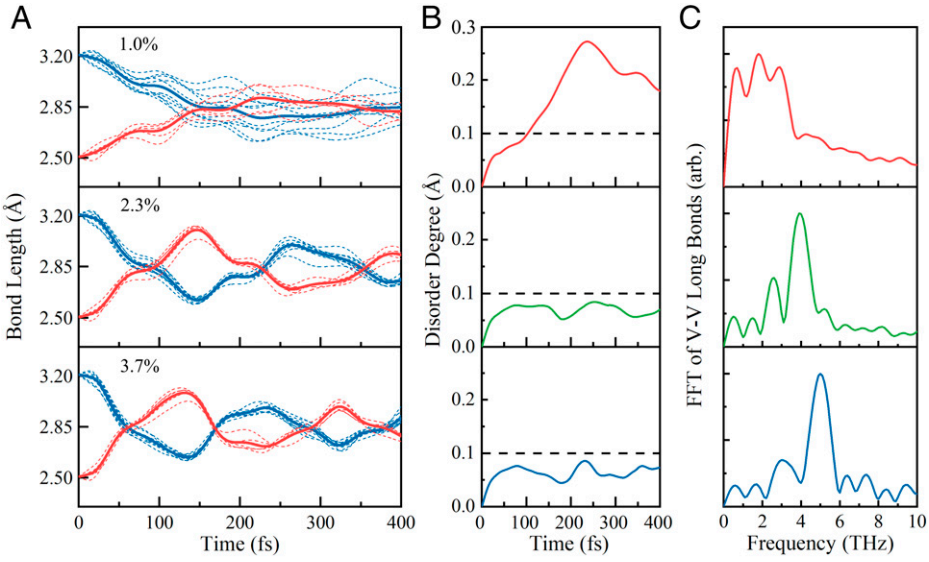

Fig. 2. Photoinduced ultrafast phase transition under different electronic excitations. (*A*) Bond-length evolution under different laser pumping conditions. The blue and red dotted lines represent the bond lengths of each long and short bond, respectively. The blue and red solid lines represent the average bond length of long and short bonds. (*B*) Disorder degree evolution at different excitations. (*C*) Phonon modes of V atoms during the phase transition, which are obtained from the normalized FFT of the average bond length of V–V bonds.

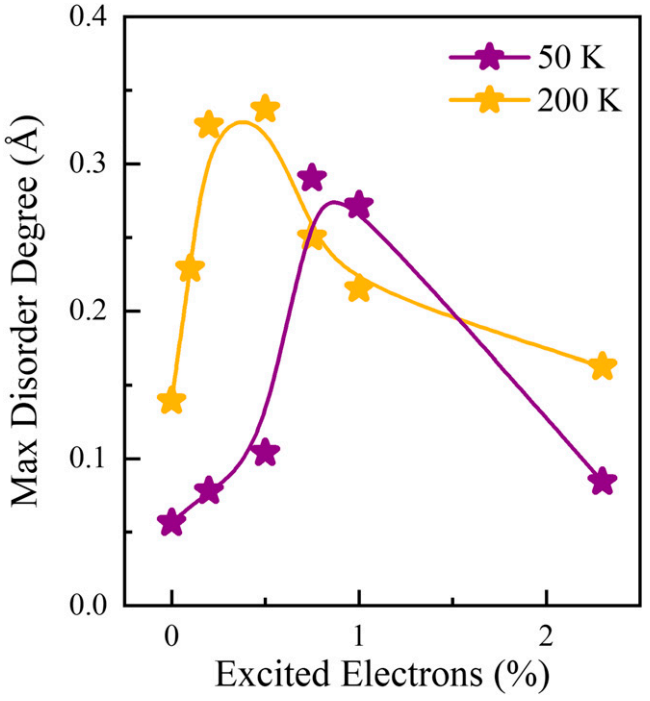

Fig. 3. The maximum disorder degree within 400 fs under different electronic excitations at 50 K and 200 K. The maximum disorder degree within 400 fs of the system reaches a maximum near the critical point of the M_1-to-R phase transition.

electronic excitation increases from 0 to 0.75% (~18 mJ/cm^2), consistent with the experimental measurement (14). According to the bond length evolutions shown in *SI Appendix*, Fig. S5*A*, the electronic excitation of 0.75% is a critical point (F_c) to make the M_1-to-R phase transition, and the strongest disorder occurs near the F_c. However, the disorder degree diminishes as the electronic excitation further increases above the F_c.

The above simulations are from the initial lattice temperature of 50 K. To explore the validity of our conclusions and compare them to the experiments at 300 K, we need to simulate the M_1-to-R phase transition at a higher temperature. First, we proceed with a Born–Oppenheimer molecular dynamic (BOMD) simulation to examine the temperature-induced phase transition. We found that in our simulations the phase transition temperature (T_c) of VO_2 is between 200 and 250 K, as shown in *SI Appendix*, Fig. S11, which is about 100 K lower than the experimental $T_c \sim 340$ K (16, 30). This difference may be due to the lower relative energy difference between the M_1 and R phases in our simulation (*SI Appendix*, Fig. S1) (34, 35). Therefore, we redo the simulations at a higher temperature of 200 K, as shown in *SI Appendix*, Fig. S12. One can see that, at 200 K, as weak as 0.2% electronic excitation (5 mJ/cm^2) can complete the M_1-to-R phase transition, whereas at 50 K the critical point F_c is ~0.75%. We can further verify the critical point will shift lower as the temperature increases in our theoretical simulations since the phonon amplitudes at higher temperatures are much larger. This phenomenon has been mentioned in many experimental works (22, 36–38). Besides, as shown in Fig. 3, we find that the larger phonon amplitudes at higher temperature results in an overall increase of the disorder under different electronic excitations. However, the transition from disorder to order as the electronic excitation increases across the critical point F_c at 200 K is the same as in the case of 50 K.

Diffraction Intensity. Furthermore, we obtain the diffraction intensity using the structure factor $F(hkl)$ (14, 20):

$$F(h,k,l) = f_V \sum_V \exp[-2\pi i q(hkl)\cdot r_V(t)] + f_O \sum_O \exp[-2\pi i q(hkl)\cdot r_O(t)] \qquad [3]$$
$$I(h,k,l) = |F(h,k,l)|^2.$$

Here, $f_V = 23$ and $f_O = 8$ denote the atomic scattering factor of V and O atoms, $q(hkl)$ is the wave vector, and $r(t)$ is the fractional coordinates of either V or O atoms at time t within the unit cell. The structure factors $F(h, k, l)$ are calculated at each time step using the atomic positions obtained from the rt-TDDFT results. Subsequently, the diffraction intensities $I(h, k, l)$ are derived from the square of the structure factors. The final results are shown in Fig. 4 and *SI Appendix*, Fig. S6. The evolution of Bragg peaks observed here indicates a structural transition from the M_1 to R phase. The $[(-131)_{M1}, (-1-13)_{M1}, (112)_{M1}, (-120)_{M1}]$ peaks in the M_1 superstructure rapidly drop to zero in intensity, and the peaks labeled $[(002)_R, (-2-23)_R]$ are present in both phases. These results are in good accord with experimental data (14), as shown in Fig. 4, although the diffraction intensities of the $(002)_R$, $(-131)_{M1}$, and $(-120)_{M1}$ peaks obtained by our simulation have some additional oscillations that are absent from the experimental observation. We think the use of a relatively small supercell (2 × 2 × 2, 96 atoms) might cause such oscillations. In such a supercell, due to its periodicity, the atoms might have some correlated movement and some random oscillation could be amplified in its diffraction spot. In actual experiments, such effects should be averaged out. However, judging by all the

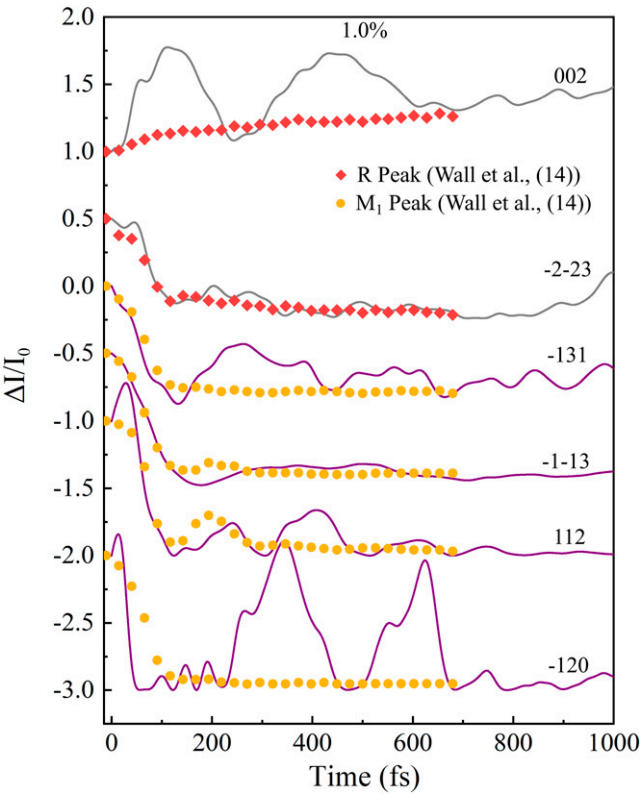

Fig. 4. Time dependence of Bragg peaks for 1.0% electronic excitation. Simulated Bragg peaks $[(002)_R, (-2-23)_R, (-131)_{M1}, (-1-13)_{M1}, (112)_{M1}, (-120)_{M1}]$ as a function of time are obtained through the structure factors (see Eq. **3**). Red diamonds and yellow circles show the relative changes in the R-phase peak and M_1-phase peak measured by X-ray diffraction experiments (14).

curves in Fig. 4, we believe our overall conclusion is still valid despite such deviation.

Microscopic Driving Force. The photoinduced phonon softening effect near the critical point is ubiquitous in a variety of PIPT systems which is usually treated as a dominant factor to induce phase transition (39–42). Indeed, structural instability is always accompanied by phonon softening effects or even more imaginary frequencies, and we discover the phonon mode softens due to the appearance of multiple phonon modes in Fig. 2*C*. On the other hand, we present an even deeper understanding by revealing the atomic driving forces for exciting these phonon modes associated with the photoexcitation-induced phase transition. The linking of atomic motions to interatomic forces is an intuitive description for the PIPT. Based on the electronic band structure, we show the occupations of photoexcited electrons and holes in Fig. 5*A*. Valence electrons from the $d_{\parallel}$ bonding states of V atoms are vertically excited to the $d_{\parallel}^{*}$ and π^{*} antibonding states in conduction bands. A strong laser fluence excites more valence electrons, but with similar orbital occupation distributions. Based on our previous theory for $IrTe_2$ (27), if n electrons are excited from bonding states to antibonding states, it will increase the free energy of the system in an amount of $\sim 2nV$, where the overlap parameter V is inversely proportional to the square of the bond length. As a result, to lower the energy of the photoexcited system, the V–V dimers need to become longer, which yields a driving force to elongate the short V–V bond along the dimer direction. Simultaneously, the occupations of excited electrons on d_{xz} and d_{yz} orbitals lead to a change of bond angles. The total driving force of the V atoms is the result of the combined action of these two forces (*SI Appendix*, Fig. S7). Note that, in an Ehrenfest dynamic, the atomic force is the minus derivative of the total energy with regard to the atomic coordinates, so it still tends to lower the total energy of the whole system. Furthermore, we explore the driving force under 1.0% and 2.3% electronic excitations. Fig. 5 *C* and *D* show the real-space distributions of photoexcited holes and electrons on $(0\bar{1}1)$ planes at the end of

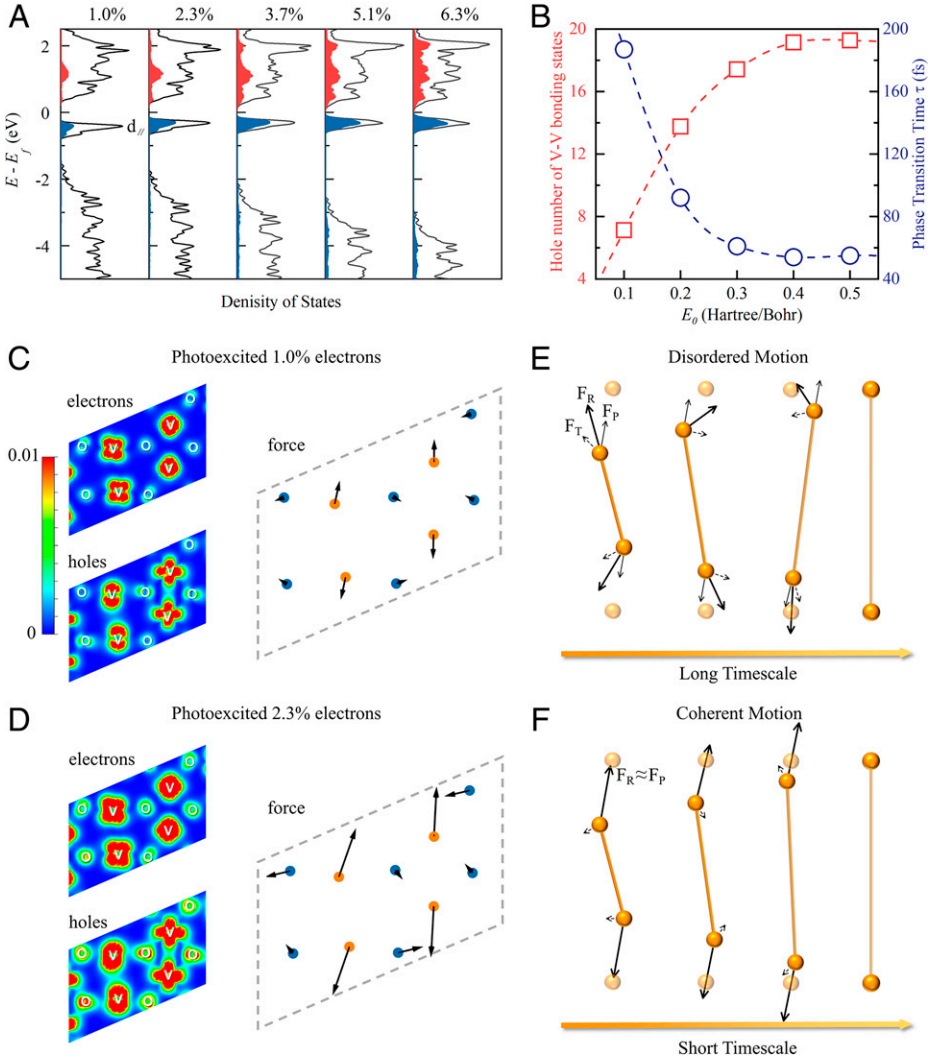

Fig. 5. The atomic microscopic driving force induced by orbital occupation changes. (*A*) Density of states of photoexcited electrons (red shaded area) and holes (blue shaded area) at different excitations. (*B*) The correlation between the holes of the V–V bonding states and the phase transition time. The red line shows the hole number of the V–V bonding states excited by different laser fluences. The blue line displays the timescale of the M_1-to-R phase transition at different laser fluences. (*C* and *D*) Real-space distributions of photoexcited holes, electrons, and driving forces on atoms caused by photoexcitation on the $(0\bar{1}1)$ plane at the end of the laser pulses (~35 fs) for the case of photoexcited 1.0% valence electrons (*C*) and the case of photoexcited 2.3% valence electrons (*D*). (*E*) Atomically disordered motion induced by multiple phonons. (*F*) Atomic coherent motion caused by strong photoexcitation. The orange balls represent a pair of V–V atoms. The F_P displays the driving force caused by photoexcitation. The dashed arrows represent the force from thermal vibrations labeled by F_T, and the black solid arrows show the resultant labeled by F_R.

the laser pulses. The photoexcited holes are mainly distributed on V atoms and between V–V dimers, primarily having a V–V bond $d_{\|}$ orbital character. The distributions of photoexcited electrons are more complicated with the occupations on V d ($d_{x^2-y^2}$, d_{xz}, and d_{yz}) and O p antibonding orbitals, corresponding to V–O antibonding and V–V antibonding characters. Notably, the carrier distributions on V atoms can be divided into two categories with a difference of 90° rotation (*SI Appendix*, Fig. S8). Overall, we prove that the photoexcited holes result in a driving force acting on V–V dimers (Fig. 5 *C* and *D*), which can induce V–V dimer dissociation (43, 44).

The driving force induced by photoexcitation can create coherent atomic motion. However, we observe a disordering behavior in the M_1-to-R phase transition at 1.0% excitation. To distinguish the different factors, we have redone the rt-TDDFT calculations with the same excitation but at the much lower lattice temperature ($T = 1$ K) to exclude the interference of thermal phonons. In 1.0% excitations, the long bonds (d_{I}) and short bonds (d_{II}) scarcely change (no M_1-to-R phase transition) within 1.0 ps because the coherent driving forces induced by the lower excitation are not enough to create the phase transition by themselves (*SI Appendix*, Fig. S9*A*). This illustrates that the structural transformation needs the assistance of thermal phonons at a low excitation level. In 2.3% excitations at $T = 1$ K, the long bonds (d_{I}) and short bonds (d_{II}) gradually become the same value at 850 fs (*SI Appendix*, Fig. S9*B*), demonstrating that, in this case, the phase transition is dominated by the coherent driving force instead of the thermal phonon. We thus have two different cases: Near the critical point (F_c), the phase transition needs the help of thermal phonons, and the atomic movement appears to be disordered; at far above the critical point (say ~3 F_c), the phase transition can be driven by coherent atomic movement alone. Thus, the atomic movement appears to be ordered and coherent.

Saturation of Hole Excitations on V–V Bonding States. Our simulations also show the disordered phase transition under 1.0% photoexcitation needs a longer timescale (~187 fs), which agrees with the experiment results in disordered PIPT (14, 25). Compared to the disordered phase transition, the PIPT can happen within 100 fs in the coherent dynamics of the V atoms along a straight trajectory from the M_1-to-R phase. Interestingly, with increasing electronic excitations, the timescale of phase transition rapidly decreases to a critical value (~55 fs) as shown in Fig. 5*B*, which is also in accordance with previous experiments (18). At the same time, the frequency of phonon mode gradually increases and reaches a saturation value (~5.5 THz). The bottleneck timescale observed at higher fluence is known as half of the period of the coherent mode in some previous experiments (10, 23). Remarkably, the timescale (~55 fs) for phase transition is far lower than the half a period (~90 fs) of the 5.5-THz phonon. This phenomenon has also been reported in one experiment (18). However, the essential reason for the phonon bottleneck and timescale saturation was not illustrated in previous literature.

For 1.0% and 2.3% excitations, photoexcited holes occupy on V–V bonding states basically. However, for 3.7%, 5.1%, and 6.3% excitations, the situations are different. The numbers of total photoexcited holes (or electrons) are 30, 41, and 50, respectively, whereas the numbers of photoexcited holes occupying on V–V bonding states are 17.4, 19.1, and 19.3 in the simulated supercell (Fig. 5 *A* and *B*). Through the distributions of photoexcited holes projected on $(0\bar{1}1)$ plane (*SI Appendix*, Fig. S10), the holes around the O atoms significantly increase with the increase of total hole distributions, while the holes around the V atoms hardly change. The effective hole number on V–V bonding states appears to be saturated, and the rest of the holes are distributed in V–O bonding states. The saturation phenomenon is caused by the band filling. According to Fermi's "golden rule," as the number of electrons on the V–V bonding state decreases it is more difficult to excite these electrons to the conduction band. At the same time, the higher laser fluence increases the probability of multiphoton absorption of electrons on the deeper valence bands (V–O bonding states) (Fig. 5*A*). As a result of this, the driving force acting on the V–V dimers is bounded by an upper limit, which determinates the fastest dissociation speed of V–V dimers.

Discussion

In the work we have observed both the coherent and disordered phase transitions for the M_1-to-R phase transition which strongly depends on the number of photoexcited carriers. This phenomenon arises from the competition between thermal vibrations and photoinduced deterministic motion of atoms. At far below the F_c, the atoms are initially in disorder motions around the equilibrium lattice sites. The excited electrons generate atomic forces pushing them toward the phase transition, and away from the equilibrium lattice sites, enhancing the disorder degree. The strongest disorder occurs around the F_c (0.75 to 1%) and embodies the larger degree of deviating a direct path from the M_1-to-R phase transition (20, 37, 45–47). This makes the disordered process happens within a longer timescale (48) where the thermal phonons are an important factor to make the phase transition possible. During the disordered process, the force direction on vanadium atoms has changed with time due to the effect of thermal phonons (Fig. 5*E*). At far above the critical point (say ~3F_c), the phase transition tends to a coherent dynamic with the coherent phonon mode, and the thermal phonons are only a small perturbation. This is caused by the increase of photoexcited electrons, which produces a larger driving force to drive the atoms toward the phase transition direction in a more deterministic way (Fig. 5*F*). The phase transition happens at a shorter timescale, corresponding to the coherent dynamics reported by the previous experiments in VO_2 (10). Although the larger phonon amplitudes at higher temperature results in an overall increase of the disorder, our conclusions are still applicable to the 200 K temperature. Of course, the phase transition speed and timescale from rt-TDDFT simulations are very difficult to make a very accurate comparison with experimental results, due to the smaller supercell size, neglect of photoinduced strain effects in our simulations, and some different experimental factors. However, we believe that our simulations have a reasonable agreement with experiments. Besides, we proved the F_c will be shifted to the lower level as the temperature increases [F_c(50 K) ~ 0.75% and F_c(200 K) ~ 0.2%], which supports the notation of temperature and photoexcitation to be cocontrol parameters for the PIPTs in VO_2 (37). With the further increase of photoinduced carriers, the coherent phonon mode gradually arrives at a saturation (~5.5 THz) which limits the atomic speed and the timescale of the phase transition (~55 fs). Such saturation has been reported experimentally for VO_2 (10, 18). Here, we have theoretically illustrated that the phenomenon is from the saturation of the photoexcited hole number on V–V bonding states. We believe these phenomena should also exist in other phase-transition materials, such as $TiSe_2$, TaS_2, and In atomic wires on Si surfaces (49–51). Our simulations not only solve the experimental

controversies but also provide a powerful view to understand the pathway of ultrafast phase transition by laser-pulse excitations.

Materials and Methods

Computational Details. We performed static calculations and rt-TDDFT simulations with the ab initio package (PWmat) (52). All calculations are based on norm-conserving pseudopotentials (53), which are generated by optimized norm-conservating Vanderbolt pseudopotentials and Perdew–Burke–Ernzerhof (PBE) exchange-correlation functions. The wave functions are expanded on a plane-wave basis with an energy cutoff of 50 Ry. V($3s^2 3p^6 4s^2 3d^3$) and O($2s^2 2p^4$) are treated as valence electrons in norm-conserving pseudopotentials. In static calculations, a PBE+U exchange-correlation with Hubbard U = 3.4 eV is used. The structure of the M_1 phase is fully relaxed by using a conventional unit cell, and an 8 × 8 × 8 k-point mesh with Monkhorst–Pack grids is used to sample the Brillouin zone. The resulting lattice constants are a = 5.67 Å, b = 4.49 Å, c = 5.32 Å, and beta = 122.47°, in good agreement with experimentally reported lattice constants in the M_1 phase at T = 298 K, a = 5.75 Å, b = 4.54 Å, c = 5.38 Å, and beta = 122.65° (54).

TDDFT Simulations. A 2 × 2 × 2 supercell (96 atoms), based on the M_1 phase fully relaxed unit cell, is used to perform rt-TDDFT simulations. To solve the problem that PBE functional will predict the wrong relative energy of the M_1 phase to the R phase, we corrected the relative energy difference by correcting the d-orbital pseudopotential of vanadium as developed in our previous work (55). The corrected relative energy is shown in *SI Appendix*, Fig. S1. In a 96-atom supercell, a 3 × 3 × 3 mesh k-point mesh with Monkhorst–Pack grids is used to sample the Brillouin zone. In the rt-TDDFT simulations (28), the time-dependent wave functions $\psi_i(t)$ are expanded by adiabatic eigenstates $\phi_j(t)$:

$$\psi_i(t) = \sum_l C_{i,l}(t)\phi_l(t) \quad [4]$$

and

$$H(t)\phi_l(t) \equiv \varepsilon_l(t)\phi_l(t) \quad [5]$$

$$H(t) \equiv H\Big(t,\ R(t),\ \rho(t)\Big). \quad [6]$$

Here, $R(t)$ represents the nuclear positions and $\rho(t)$ represents the charge density. In Eq. **4**, the evolution of the wave functions $\psi_i(t)$ is changed to the evolution of the coefficient $C_{i,l}(t)$. In Eq. **5**, a linear-time-dependent Hamiltonian is applied to represent the time dependence of the Hamiltonian within a time step. Thus, our rt-TDDFT simulation has a much larger time step (0.1 fs) than the conventional rt-TDDFT (subattosecond).

To mimic photoexcitation, we introduce a uniform A field in reciprocal space (56),

$$H = 1/2(-i\nabla + \boldsymbol{A})^2 = 1/2(-i\nabla_x + A_x)^2 + 1/2(-i\nabla_y + A_y)^2 + 1/2(-i\nabla_z + A_z)^2 . \quad [7]$$

The time–space external field can be described as a Gaussian shape in Eq. **1**.

Data Availability. All study data are included in the article and/or *SI Appendix*.

ACKNOWLEDGMENTS. The work in China was supported by the Key Research Program of Frontier Sciences, Chinese Academy of Sciences (CAS) under grant ZDBS-LY-JSC019, CAS Project for Young Scientists in Basic Research under grant YSBR-026, the Strategic Priority Research Program of the CAS under grant XDB43020000, and the National Natural Science Foundation of China under grants 11925407 and 61927901. L.-W.W. was supported by the Director, Office of Science, the Office of Basic Energy Sciences, Materials Sciences and Engineering Division of the US Department of Energy through the theory of material (KC2301) program under contract DEAC02-05CH11231.

1. H. Y. Hwang *et al.*, Emergent phenomena at oxide interfaces. *Nat. Mater.* **11**, 103–113 (2012).
2. S. I. Ideta *et al.*, Ultrafast dissolution and creation of bonds in $IrTe_2$ induced by photodoping. *Sci. Adv.* **4**, eaar3867 (2018).
3. C. W. Nicholson *et al.*, Beyond the molecular movie: Dynamics of bands and bonds during a photoinduced phase transition. *Science* **362**, 821–825 (2018).
4. A. Zong *et al.*, Evidence for topological defects in a photoinduced phase transition. *Nat. Phys.* **15**, 27–31 (2019).
5. J. Zhang *et al.*, Photoexcitation induced quantum dynamics of charge density wave and emergence of a collective mode in 1T-TaS_2. *Nano Lett.* **19**, 6027–6034 (2019).
6. W.-H. Liu, J.-W. Luo, S.-S. Li, L.-W. Wang, The critical role of hot carrier cooling in optically excited structural transitions. *npj Comput. Mater.* **7**, 117 (2021).
7. C. Lian, S. J. Zhang, S. Q. Hu, M. X. Guan, S. Meng, Ultrafast charge ordering by self-amplified exciton-phonon dynamics in $TiSe_2$. *Nat. Commun.* **11**, 43 (2020).
8. X.-P. Wang *et al.*, Time-dependent density-functional theory molecular-dynamics study on amorphization of Sc-Sb-Te alloy under optical excitation. *npj Comput. Mater.* **6**, 31 (2020).
9. N.-K. Chen *et al.*, Directional forces by momentumless excitation and order-to-order transition in Peierls-distorted solids: The case of GeTe. *Phys. Rev. Lett.* **120**, 185701 (2018).
10. A. Cavalleri, T. Dekorsy, H. H. W. Chong, J. C. Kieffer, R. W. Schoenlein, Evidence for a structurally-driven insulator-to-metal transition in VO_2: A view from the ultrafast timescale. *Phys. Rev. B* **70**, 161102 (2004).
11. P. Beaud *et al.*, A time-dependent order parameter for ultrafast photoinduced phase transitions. *Nat. Mater.* **13**, 923–927 (2014).
12. A. Cavalleri *et al.*, Femtosecond structural dynamics in VO_2 during an ultrafast solid-solid phase transition. *Phys. Rev. Lett.* **87**, 237401 (2001).
13. L. X. Yang *et al.*, Ultrafast modulation of the chemical potential in BaFe2As2 by coherent phonons. *Phys. Rev. Lett.* **112**, 207001 (2014).
14. S. Wall *et al.*, Ultrafast disordering of vanadium dimers in photoexcited VO_2. *Science* **362**, 572–576 (2018).
15. L. X. Yang *et al.*, Bypassing the structural bottleneck in the ultrafast melting of electronic order. *Phys. Rev. Lett.* **125**, 266402 (2020).
16. E. Strelcov, Y. Lilach, A. Kolmakov, Gas sensor based on metal-insulator transition in VO_2 nanowire thermistor. *Nano Lett.* **9**, 2322–2326 (2009).
17. B.-J. Kim *et al.*, Temperature dependence of the first-order metal-insulator transition in VO_2 and programmable critical temperature sensor. *Appl. Phys. Lett.* **90**, 023515 (2007).
18. S. Wall *et al.*, Tracking the evolution of electronic and structural properties of VO_2 during the ultrafast photoinduced insulator-metal transition. *Phys. Rev. B* **87**, 115126 (2013).
19. B. T. O'Callahan *et al.*, Inhomogeneity of the ultrafast insulator-to-metal transition dynamics of VO_2. *Nat. Commun.* **6**, 6849 (2015).
20. P. Baum, D. S. Yang, A. H. Zewail, 4D visualization of transitional structures in phase transformations by electron diffraction. *Science* **318**, 788–792 (2007).
21. A. Pashkin *et al.*, Ultrafast insulator-metal phase transition in VO_2 studied by multiterahertz spectroscopy. *Phys. Rev. B* **83**, 195120 (2011).
22. C. Kübler *et al.*, Coherent structural dynamics and electronic correlations during an ultrafast insulator-to-metal phase transition in VO_2. *Phys. Rev. Lett.* **99**, 116401 (2007).
23. S. Wall *et al.*, Ultrafast changes in lattice symmetry probed by coherent phonons. *Nat. Commun.* **3**, 721 (2012).
24. S. Gerber *et al.*, Femtosecond electron-phonon lock-in by photoemission and x-ray free-electron laser. *Science* **357**, 71–75 (2017).
25. M. R. Otto *et al.*, How optical excitation controls the structure and properties of vanadium dioxide. *Proc. Natl. Acad. Sci. U.S.A.* **116**, 450–455 (2019).
26. V. R. Morrison *et al.*, A photoinduced metal-like phase of monoclinic VO_2 revealed by ultrafast electron diffraction. *Science* **346**, 445–448 (2014).
27. W.-H. Liu, J.-W. Luo, S.-S. Li, L.-W. Wang, Microscopic force driving the photoinduced ultrafast phase transition: Time-dependent density functional theory simulations of $IrTe_2$. *Phys. Rev. B* **102**, 184308 (2020).
28. Z. Wang, S.-S. Li, L.-W. Wang, Efficient real-time time-dependent density functional theory method and its application to a collision of an ion with a 2D material. *Phys. Rev. Lett.* **114**, 063004 (2015).
29. F. J. Morin, Oxides which show a metal-to-insulator transition at the Neel temperature. *Phys. Rev. Lett.* **3**, 34–36 (1959).
30. M. Imada, A. Fujimori, Y. Tokura, Metal-insulator transitions. *Rev. Mod. Phys.* **70**, 1039–1263 (1998).
31. J. B. Goodenough, The two components of the crystallographic transition in VO_2. *J. Solid State Chem.* **3**, 490–500 (1971).
32. N. B. Aetukuri *et al.*, Control of the metal–insulator transition in vanadium dioxide by modifying orbital occupancy. *Nat. Phys.* **9**, 661–666 (2013).
33. W. A. Harrison, *Elementary Electronic Structure* (World Scientific, 2004).
34. F. Pintchovski, W. S. Glaunsinger, A. Navrotsky, Experimental study of the electronic and lattice contributions to the VO_2 transition. *J. Phys. Chem. Solids* **39**, 941–949 (1978).
35. J. H. Park *et al.*, Measurement of a solid-state triple point at the metal–insulator transition in VO_2. *Nature* **500**, 431–434 (2013).
36. Z. Tao *et al.*, Decoupling of structural and electronic phase transitions in VO_2. *Phys. Rev. Lett.* **109**, 166406 (2012).
37. Z. Tao *et al.*, The nature of photoinduced phase transition and metastable states in vanadium dioxide. *Sci. Rep.* **6**, 38514 (2016).
38. C. Xu *et al.*, VO_2 does not host a photoinduced long-lived monoclinic metallic phase. arXiv [Preprint] (2022). https://arxiv.org/abs/2203.09776 (Accessed 20 March 2022).
39. K. Appavoo *et al.*, Ultrafast phase transition via catastrophic phonon collapse driven by plasmonic hot-electron injection. *Nano Lett.* **14**, 1127–1133 (2014).
40. Z. Sun, A. J. Millis, Transient trapping into metastable states in systems with competing orders. *Phys. Rev. X* **10**, 021028 (2020).
41. F. Zhou *et al.*, Nonequilibrium dynamics of spontaneous symmetry breaking into a hidden state of charge-density wave. *Nat. Commun.* **12**, 566 (2021).
42. A. Zong *et al.*, Role of equilibrium fluctuations in light-induced order. *Phys. Rev. Lett.* **127**, 227401 (2021).
43. X. Yuan, Y. Zhang, T. A. Abtew, P. Zhang, W. Zhang, VO_2: Orbital competition, magnetism, and phase stability. *Phys. Rev. B* **86**, 235103 (2012).
44. M. van Veenendaal, Ultrafast photoinduced insulator-to-metal transitions in vanadium dioxide. *Phys. Rev. B* **87**, 235118 (2013).
45. A. Sood *et al.*, Universal phase dynamics in VO_2 switches revealed by ultrafast operando diffraction. *Science* **373**, 352–355 (2021).
46. P. Jean-Paul, Basic aspects of the metal–insulator transition in vanadium dioxide VO_2: A critical review. *C. R. Phys.* **22**, 37–87 (2021).

47. S. Xiaoyi, S. Shuaishuai, R. Chong-Yu, Toward nonthermal control of excited quantum materials: Framework and investigations by ultrafast electron scattering and imaging. *C. R. Phys.* **22**, 15–73 (2021).
48. A. Zong *et al.*, Dynamical slowing-down in an ultrafast photoinduced phase transition. *Phys. Rev. Lett.* **123**, 097601 (2019).
49. M. Eichberger *et al.*, Snapshots of cooperative atomic motions in the optical suppression of charge density waves. *Nature* **468**, 799–802 (2010).
50. C. Sohrt, A. Stange, M. Bauer, K. Rossnagel, How fast can a Peierls-Mott insulator be melted? *Faraday Discuss.* **171**, 243–257 (2014).
51. T. Frigge *et al.*, Optically excited structural transition in atomic wires on surfaces at the quantum limit. *Nature* **544**, 207–211 (2017).
52. W. L. Jia *et al.*, The analysis of a plane wave pseudopotential density functional theory code on a GPU machine. *Comput. Phys. Commun.* **184**, 9–18 (2013).
53. D. R. Hamann, Optimized norm-conserving Vanderbilt pseudopotentials. *Phys. Rev. B* **88**, 085117 (2013).
54. J. M. Longo, P. Kierkega, A refinement of the structure of VO_2. *Acta Chem. Scand.* **24**, 420–426 (1970).
55. W.-H. Liu, J.-W. Luo, S.-S. Li, L.-W. Wang, Impurity diffusion induced dynamic electron donors in semiconductors. *Phys. Rev. B* **100**, 165203 (2019).
56. Z. Chen, L.-W. Wang, Role of initial magnetic disorder: A time-dependent ab initio study of ultrafast demagnetization mechanisms. *Sci. Adv.* **5**, eaau8000 (2019).